

Article

# Numerical Investigation on Heat-Transfer and Hydromechanical Performance inside Contaminant-Insensitive Sublimators under a Vacuum Environment for Spacecraft Applications

Lijun Gao <sup>1</sup>, Yunze Li <sup>1,2,3,\*</sup> , Huijuan Xu <sup>1</sup>, Xin Zhang <sup>1</sup>, Man Yuan <sup>3,4</sup> and Xianwen Ning <sup>5</sup>

<sup>1</sup> Advanced Research Center of Thermal and New Energy Technologies, Xingtai Polytechnic College, Xingtai 054035, China; gaoli\_jun@foxmail.com (L.G.); xuhuijuan\_xpc@163.com (H.X.); zx\_xtpc@163.com (X.Z.)

<sup>2</sup> School of Aeronautic Science and Engineering, Beihang University, Beijing 100191, China

<sup>3</sup> Institute of Engineering Thermophysics, North China University of Water Resources and Electric Power, Zhengzhou 450045, China; Manyuan@ncwu.edu.cn

<sup>4</sup> School of Electric Power, North China University of Water Resources and Electric Power, Zhengzhou 450045, China

<sup>5</sup> Beijing Key Laboratory of Space Thermal Control Technology, Beijing Institute of Space Systems Engineering, Beijing 100094, China; ningxianwen@163.com

\* Correspondence: liyunze@buaa.edu.cn; Tel.: +86-10-8233-8778; Fax: +86-10-8231-5350

Received: 11 November 2019; Accepted: 28 November 2019; Published: 29 November 2019



**Abstract:** The contaminant-insensitive sublimator (CIS) is a novel water sublimator in development, which uses two porous substrates to separate the sublimation point from the pressure-control point and provide long-life effective cooling for spacecraft. Many essential studies need to be carried out in the field. To overcome the reliability issues such as ice breakthrough caused by large temperature or pressure differences, the CIS development unit model, the mathematical models of heat and mass transfer and the evaluation coefficient have been established. Numerical investigations have been implemented aiming at the impacts of physical properties of porous substrate, physical properties of working fluid, orifice layouts and orifice-structure parameters on the characteristics of flow field and temperature field. The numerical investigation shows some valuable conclusion, such as the temperature uniformity coefficient at the bottom surface of the large pore substrate is 0.997669 and the pressure uniformity coefficient at the same surface is 0.85361267. These numerical results can provide structure and data reference for the CIS design of lunar probe or spacesuit.

**Keywords:** contaminant-insensitive sublimator; porous substrate; feed-water; working fluid; temperature field; flow field

## 1. Introduction

With the rapid development of the space industry, the frequency of space activities, which include deep-space exploration, extravehicular activities and so on, will be higher and higher [1–5]. However, a lot of waste heat is generated when spacecraft are in working status, and solving the problem of the heat dissipation of spacecraft and equipment such as lunar probes and spacesuits has accordingly become the focus of the powerful countries in space exploration [6–8]. Space radiators and water sublimators are two types of necessary heat sinks for space cooling [6,9]. Space radiators are the passive cooling sources used in most space applications, but, they have some disadvantages such as a limited dissipation power and the low power-mass ratio. Conversely, water sublimators can be

used as a supplementary heat sink of space radiators to dissipate the peak waste heat, and can also be used as the exclusive heat sink of small spacecraft in a warm thermal environment or with strict weight limits for cooling sources, for instance, when the spacecraft is operating in and near the direct sunlight spot in low lunar orbit [10–13]. At this time, the use of water sublimators as heat sinks has been recognized by the powerful countries in space exploration. When China's chang'e-5 lunar lander worked during the day, a large amount of waste heat generated in a short period of time was dissipated through a water sublimator.

Water sublimators are phase change heat dissipation devices, which make full use of the fact the high vacuum pressure in space is far lower than the pressure of the triple point of water to realize the phase change process from liquid to solid to gas of water. This process absorbs a large amount of waste heat from the spacecraft and dissipates it into space with leaving steam. The advantages of the water sublimator such as simplicity, light weight, small volume, small power consumption, high-efficiency, reliable operation in zero gravity and under the condition of thermal load variation are very suitable for space cooling. Sublimators have been successfully used to dissipate heat from various spacecraft and life support systems, such as the Apollo lunar module and extravehicular mobility unit (EMU), the International Space Station portable life support system (PLSS), and the European space agency's Hermes spacesuit [14–16]. Currently, the x-38 water sublimator, the CIS for the x-38 crew return vehicle, as well as the sublimator driven coldplate (SDC) and the integrated sublimation driven coldplate (ISDC) for the Orion manned spacecraft and Altair lunar module represent the highest level of sublimator use.

In the past few decades, many researchers have done lots of investigations on sublimators. These studies mainly focused on the feasibility verification, heat-and-mass transfer performance, utilization rate of feed-water (FW) and so on, which are shown as follow. Planert et al. developed a new sublimator for the European Space Suit, which employed a novel porous plate fabricated from stainless steel, and executed tests to certify the technical feasibility of the design concept [17]. Tongue et al. build two sublimators for the X-38 program, and described sublimator performance at both component and system level and the ground test data at CRV conditions [18,19]. Based on JSC x-38 design, Leimkuehler et al. proposed a kind of CIS which used a large pore porous plate to make the CIS less sensitive to contaminants, and described the design, fabrication, and testing of the CIS Engineering Development Unit (EDU) [20,21]. Leimkuehler et al. depicted the design of an engineering development unit of the SDC to demonstrate the SDC concept [22]. To better understand the basic operational principles and to validate the analytical methods used for the SDC development, Sheth et al. outlined the test results of the SDC Engineering Development Unit [23]. Leimkuehler et al. implemented the starting utilization test on the x-38 water sublimator and CIS, and studied the FW consumption efficiency under cyclic conditions [24,25]. Sheth et al. tested the performance of a SDC in a vacuum chamber, and the test data was used to establish the relevant thermal math models [26]. Sheth also studied the influence of the transient start and stop process of sublimator on the FW's utilization in the cyclical topping mode [27]. Leimkuehler et al. tested an ISDC test article in a vacuum chamber, and used the testing results to demonstrate proof of concept for the ISDC [28]. Wang et al. investigated the heat and mass transfer of a porous plate water sublimator with constant heat flux boundary condition via simulation and experiment [29].

What's more, the porous substrate is the critical core component of sublimator because of its serious influence on the process of the heat and mass transfer in the sublimator and the phase-change location. The issues of the phase change and the heat and mass transfer in porous substrates have been studied in the previous literature, and these studies are useful to sublimator research and are classified into two categories, described as follows. The first category is the influence of structure parameters, flow characteristics, fluid properties, physical parameters and heat-transfer characteristics on heat-and-mass transfer performance in porous substrate [30–36]. Hanlon et al. researched the influences of the thin film evaporation, the particle size, the porosity, and the wick structure thickness on the evaporation heat transfer in sintered wick structure based on a two-dimensional heat-transfer

model [37]. The heat transfer performance of a solid/liquid phase-change thermal energy storage system that includes porous metal foam was investigated by Siahpush et al. through a detailed experimental study [38]. Wang et al. used the variable time step finite-difference method to solve the governing equation of the drying process numerically, and studied the sublimation condensation phenomenon in the process of microwave freeze drying [39]. Another category is the establishment of mathematical models for phase-change processes in porous substrate [40–46]. Farid has established unsteady-state heat conduction equations for phase-change processes such as melting, solidification, microwave thawing, spray-drying, and freeze-drying, and developed two different numerical solutions for sharp interfaces and materials undergoing phase transformation within a certain temperature range [47]. In order to solve the nonhomogeneous problem from the moving phase-change interface, Leung et al. used a Green function to solve the problem of phase-change heat transfer during thawing of frozen food theoretically [48]. Rattanadecho et al. studied the freezing problem of water-saturated porous media in rectangular cavity subjected to multiple heat sources by numerical method [49]. In order to predict the freeze-drying kinetics of the multi-dimensional sublimation process in a product, Nakagawa et al. established a mathematical model consisting of classical heat and mass transfer equations, and solved it by assuming the porous media transport model with a distributed sublimation front [50].

The studies reported in the literature investigated feasibility verification, heat-and-mass transfer performance, utilization rate of FW and location of sublimation for all kinds of sublimators by the test method, and studied the phase-change process of heat and mass transfer in porous media. However, slightly different, the working process of the water sublimator involves multi-physics coupling in the process of the heat and mass transfer inside porous media, forced convection and water phase-change process in the triple point. In addition, the numerical analysis of the internal pressure field, velocity field and temperature field of the CIS is rarely mentioned in the present.

Based on these facts, this paper researches many factors that affect the CIS. Primarily, the effect of Physical parameters of porous substrates in the CIS, the Flow characteristics and fluid properties, the layout of the orifice, and the Structure parameters of the orifice on the heat-transfer and hydromechanical performance inside CIS under vacuum environment for spacecraft applications were studied numerically. These works have not been done by domestic and foreign researchers, but they play an important role in the steady-state study of the CIS. Some conclusions with reference price value were acquired.

## 2. Function, Layout, Mathematic Model and Simulation Parameters of CIS

### 2.1. Function and Physical Model of CIS

#### 2.1.1. Operating Mechanism

The structure comparison between the general sublimator and the CIS is depicted in Figure 1. One of the drawbacks of the general sublimator is that it is sensitive to any contaminants dissolved in the FW, which can build up and then block the micron-sized pores in the small pore substrate. To improve the working performance of sublimator, the CIS is developed, which uses a small pore disk to control the FW's working pressure and applies large pore substrate as the sublimation site. The large pore substrate is insensitive to the contaminants dissolved in the FW [20,21].

Figure 2a shows a CIS cooling system, which includes a thermal loop and a FW loop. The water circulating in the thermal loop is named working fluid (WF), and the dissipative water in the FW loop is denoted as FW. The thermal loop collects waste heat from the spacecraft application and transmits it to CIS, and the FW provided by the FW loop freezes firstly and then absorbs the waste heat in the CIS and changes into steam which is discharged to the space environment.

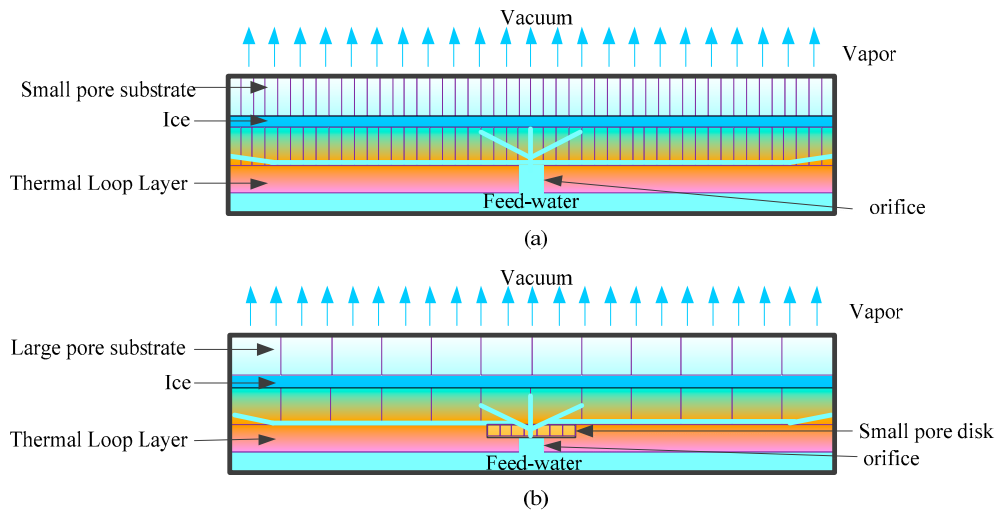


**Figure 1.** Structure comparison between the CIS and the general sublimator. (a) Structure of the general sublimator. (b) Structure of the CIS.

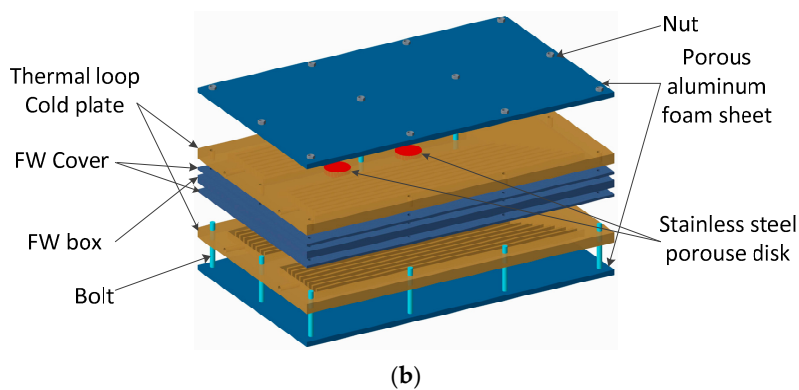
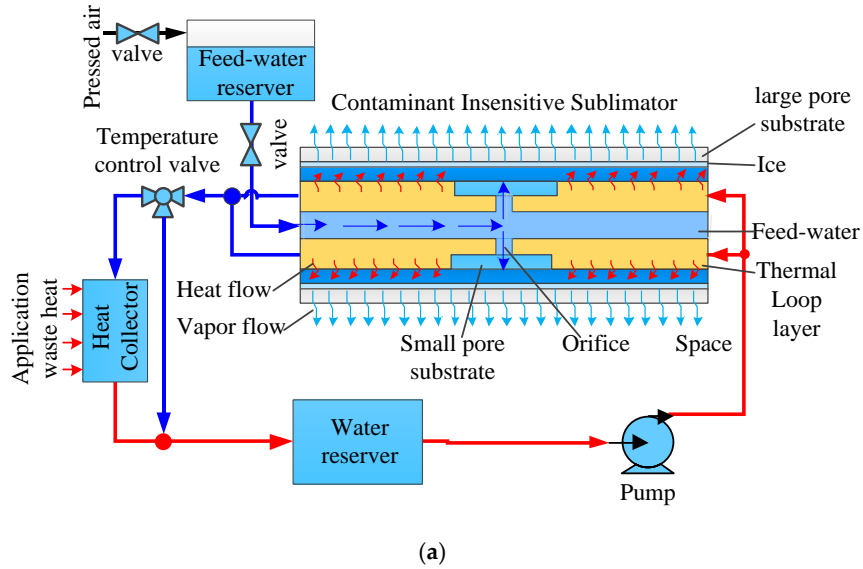


**Figure 2.** The heat dissipated method with the CIS as heat sink. (a) Heat dissipation through CIS cooling system. (b) The structure of the CIS.

As the key component of the CIS cooling system, the CIS is a planar symmetric structure, as shown in Figure 2a,b. It is mainly composed of large pore substrate, small pore substrate, thermal loop layer and FW layer. The large pore substrates of the CIS are the porous aluminum foam sheets (PAFS),

and the small pore substrates are the stainless steel porous disks (SSPD). The thermal loop layers are two cold plates (CP) with inner fins, which are also known as heat exchange, and the water layer is designed as a box form. The FW covers are brazed between the FW layer and the thermal loop layer to separate the working fluid in the thermal loop from the FW. To transfer mass and heat fluently, the large pore substrates and the small pore substrates are fastened on the FW cover by bolts.

The key problem of CIS design is to how control the position of the sublimation. In order to control the sublimation of the FW at a suitable height in the large pore substrate, the working pressure of the FW in CIS must be controlled strictly. For the purpose, two kinds of porous substrates are adopted in CIS. The small pore substrates are mainly used to generate large liquid resistance and form a large pressure drop, so as to realize pressure control and distribution of the FW. The large pore substrate chiefly provides a phase change site to overcome the blockage of small pores by dissolved contaminants. The FW flows through the FW layer, the orifice, and to the small pore substrate where the FW is diverged by the small pore substrate into the large pore substrate. At the large pore substrate, the FW is exposed to space vacuum where the pressure is below the triple point pressure, as well as the temperature is much lower than that of the triple point, then freezes. The ice absorbs the waste heat of the aircraft transferred by the thermal loop layer and directly sublimates into steam, which cools the WF in the thermal loop layer.

### 2.1.2. The Development Unit of the CIS

Because CIS is a planar symmetric structure, only half of the symmetric structure is select as the development unit to study for saving the computation which is shown in Figure 3a. The PAFS is mounted on the outermost layer and is 3 mm thick. Two holes are drilled on the back of the CP to install two SSPDs with a thickness of 1.5 mm. The layout of the SSPD is shown in Figure 3d. The structure of the orifices connecting the FW box to the SSPD is drawn in Figure 3b. The inside liquid channels of the CP is shown in Figure 3c. The diameters of the inlet and outlet of the CP are all set as 4 mm. The WF of the thermal loop is located in the cavity inside the CP. The FW's fluid domain is imbedded in the FW box and the orifice.

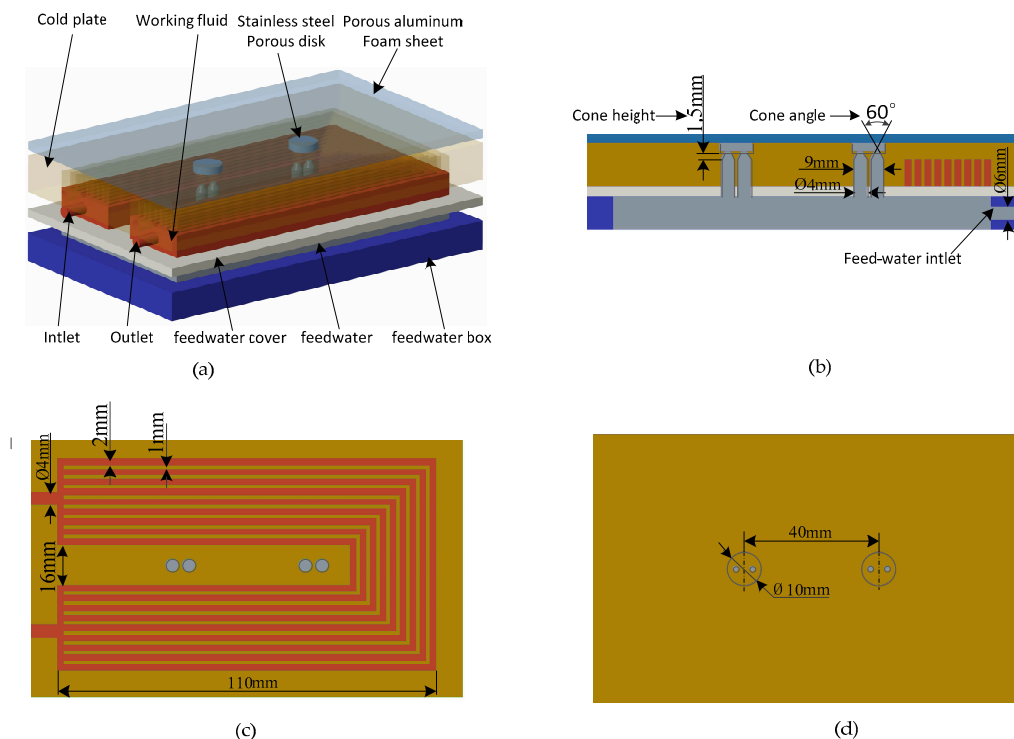


**Figure 3.** Diagram of the CIS's development unit. (a) Model of the CIS; (b) Structure of the orifice; (c) cooling channels inside the CP; (d) mounting position of the SSPD.

## 2.2. Mathematic Model of CIS

### 2.2.1. Assumption

To develop the mathematical model in the following sections, the main assumptions are made as follows:

- 1) It is considered that the FW in the micron pores of the large pore plate can freeze quickly once the vacuum environment decreases to the triple point of water.
- 2) Assume that the water sublimation phase transition occurs only in the large pore substrate.
- 3) Neglect the convective heat transfer between FW and the other components of the sublimator, especially when flowing in porous substrate.
- 4) Suppose that the micron pores of the large pore substrate and the small pore substrate are filled with the FW.

### 2.2.2. Heat and Mass Transfer Model in Fluid Domain

#### 1) Governing equations of the fluid domain

We assumed that the working fluid that flows through the CD in the thermal loop and the FW is incompressible and the gravity is set as zero in microgravity environment. The complete convection heat transfer equations include the continuity equation, momentum equation and energy equation as follows:

Continuity equation:

$$\rho_w \nabla \cdot u_w = 0 \quad (1)$$

Momentum equation:

$$\rho_w \frac{\partial u_w}{\partial t} + \rho_w (u_w \cdot \nabla) u_w = -\nabla p + \mu \nabla^2 u_w + F_w \quad (2)$$

Energy equation:

$$\rho_w C_w \frac{\partial T}{\partial t} + \rho_w C_w u_w \cdot \nabla T + \nabla \cdot q_w = Q_w \quad (3)$$

$$q_w = -k_w \nabla T \quad (4)$$

where  $\rho_w$  is the fluid density,  $u_w$  is the fluid velocity vector at each point,  $t$  is the time,  $p$  is the pressure,  $\mu$  is the dynamic viscosity,  $F_w$  is the volume force vector,  $C_w$  is the fluid specific heat capacity,  $T$  is the absolute temperature,  $q_w$  is the heat flux vector,  $Q_w$  is the heat source (or sink),  $k_w$  is the fluid thermal conductivity.

#### 2) Heat Equilibrium

When the water sublimator works in the sublimation mode, waste heat is transferred to the water sublimator through the WF flowing through the thermal-loop CP, and then the heat is dissipated by the combined sublimation. According to the heat equilibrium and the previous assumption, the following equations can be obtained:

Waste heat:

$$\Phi_{ws} = m_c C_w (T_{in} - T_{out}) \quad (5)$$

Latent heat from sublimation:

$$\Phi_l = m_f (H_{su} - H_{so}) \quad (6)$$

Mass flow rate:

$$m_f = \frac{\Phi_{ws} = \Phi_l}{\frac{m_c C_w (T_{in} - T_{out})}{H_{su} - H_{so}}} \quad (7)$$

where  $\Phi_{ws}$  is the heat transfer rate of the waste heat,  $m_c$  is the mass flow rate of the WF,  $T_{in}$  is the absolute temperature of the WF at the inlet of the thermal-loop CP,  $T_{out}$  is the absolute temperature of the WF at the outlet of the thermal-loop CP,  $\Phi_l$  is the heat transfer rate of latent heat from sublimation,  $m_f$  is the mass flow rate of the FW,  $H_{sl}$  is the latent heat of sublimation,  $H_{so}$  is the latent heat of solidification.

### 2.2.3. Heat Transfer Model in Solid Domain

The metal solid components of the water sublimator include thermal-loop CP, FW cover and FW box, which are brazed together to have better thermal conductivity. The thermal conductivity of the components is the main factor affecting the outlet temperature of the WF when the inlet WF temperature is fixed. Therefore, it is necessary to pay attention to the temperature field distribution in the solid domain of the water sublimator. The three-dimensional unsteady heat conduction equation in the cartesian coordinate system is shown as follows:

$$\rho_{so}C_{so}\frac{\partial T_{so}}{\partial t} = k_{so}\nabla^2 T_{so} + Q_{so} \quad (8)$$

where  $\rho_{so}$  is the density of the solid components,  $C_{so}$  is the specific heat capacity of each material,  $T_{so}$  is the temperature field,  $k_{so}$  is the solid thermal conductivity,  $Q_{so}$  is the heat source power.

### 2.2.4. Heat and Mass Transfer Model in Porous Substrate

The large pore substrate and small pore substrate located between the heat source and the heat sink are the important channels for heat and mass transfer. Based on the previous assumption, when the water sublimator is in operating state, the porous substrate is filled with water and belongs to saturated porous medium. Its effective coefficient can be obtained by volume average method. The governing equations for heat and mass transfer in saturated porous media are shown below.

Continuity equation:

$$\rho_w \nabla \cdot u_w = 0 \quad (9)$$

When water flows in the porous substrate, the Reynolds number is less than 10 and it is laminar flow. Therefore, the relationship between velocity and pressure and viscous force is expressed by darcy's law, where the permeability identified by  $\kappa$  is a function of the porosity and the pore size [51,52].

$$u_w = -\frac{\kappa}{\mu} \nabla p \quad (10)$$

$$\kappa = \frac{d^2 \varepsilon^3}{180(1 - \varepsilon)^2} \quad (11)$$

Energy equation:

$$\rho_{eff}c_{eff}\frac{\partial T}{\partial t} = k_{eff}\nabla T + Q \quad (12)$$

$$\rho_{eff} = (1 - \varepsilon)\rho_{po} + \varepsilon\rho_w \quad (13)$$

$$C_{eff} = (1 - \varepsilon)C_{po} + \varepsilon C_w \quad (14)$$

$$k_{eff} = (1 - \varepsilon)k_{po} + \varepsilon k_w \quad (15)$$

where  $\mu$  is the dynamic viscosity of the fluid,  $d$  is the pore diameter,  $\varepsilon$  is the porosity,  $\rho_{eff}$  is the effective density,  $\rho_{po}$  is the density of the porous matrix,  $C_{eff}$  is the effective specific heat capacity,  $C_{po}$  is the specific heat capacity of the porous matrix,  $k_{eff}$  is the effective thermal conductivity,  $k_{po}$  is the thermal conductivity of the porous matrix.

### 2.2.5. Temperature Uniformity and Pressure Uniformity Evaluation Models

Two parameters are defined to evaluate the temperature uniformity and the pressure uniformity of the CIS's sections. The temperature uniformity is defined as

$$\alpha = 1 - \frac{T_{\max} - T_{\min}}{T_{av}} \quad (16)$$

where  $T_{\max}$  and  $T_{\min}$  are the maximum temperature and the minimum temperature on the sections of the CIS,  $T_{av}$  is the average temperature on the corresponding sections.

The pressure uniformity is indicated in the form of:

$$\beta = 1 - \frac{p_{\max} - p_{\min}}{p_{av}} \quad (17)$$

where  $p_{\max}$ ,  $p_{\min}$  and  $p_{av}$  are the maximum pressure, the minimum pressure and the average pressure on the sections of the CIS respectively. A larger value for both the two parameters means that ice breakthrough is likely to occur.

### 2.2.6. Compensatory Coefficient Evaluation Model

The compensatory coefficient is used to evaluate the effective availability of operating power of the FW loop in dissipating the waste heat from the space applications, which is denoted as:

$$\eta = \frac{\Delta p G_1}{m_c C_p (T_{in} - T_{out})} \quad (18)$$

where  $G_1$  is the FW's flow rate,  $\Delta p$  is the FW's pressure difference between the inlet and the outlet of the CP in the CIS. If the compensation coefficient is small, it signifies that the FW loop consumes less power to dissipate the same waste heat from the space application.

## 2.3. Simulation Parameters for CIS

The simulation is calculated by the COMSOL Multiphysics software, which is widely applied in various fields of scientific research and engineering calculation. Based on finite element mesh model, COMSOL Multiphysics finished the simulation study of this paper by solving partial differential equation or equations. According to the previous physical model, the study in this paper involves three physical fields, namely, the laminar flow physical field of the thermal loop, the laminar flow physical field of the FW loop and the solid heat transfer physical field.

### 2.3.1. Boundary Condition Setting

In the CIS, the FW's mass flow rate  $m_f$ , a most important parameter, can be calculated through Equation (7) according to energy conservation. The waste heat power that needs to be discharged by the CIS is transferred by the WF in the thermal loop, and the power is 400 W. The inlet flow velocity of the CP in the thermal loop is 0.761 m/s calculated through Equation (5) when the WF's temperature drop is set at 5 K and the waste-heat power is a half of 400 W, the inlet temperature is 290.15 K, and the outlet pressure of the CP is set as 0 Pa. The inlet flow velocity of the FW is 0.00283 m/s, the inlet temperature is 283.15 K. In accordance with the assumption, the upper surface of the PAFS is considered to be the site of water sublimation, therefore, the pressure is set to 610 Pa and the surface temperature is set to 273.15 K [23,26,28]. The remaining surfaces are adiabatic.

### 2.3.2. Thermo-Physical Properties

The thermo-physical properties of CIS used for the investigation are listed in Table 1.

**Table 1.** Thermo-physical properties of the CIS, and other materials [21,22,24,29].

-	Density (kg/m <sup>3</sup> )	Specific Heat (J/kg K)	Thermal Conductivity (W/m K)	Component
Stainless steel	7930	500	17	CP, FW cover, FW box, SSPD
Aluminum foam	2700	896	180	PAFS
Water	1000	4212	0.551	FW, WF

### 2.3.3. Factors Affecting CIS's Performance

#### 1) Physical parameters of porous substrates

Porous substrate is key components of the CIS. The parameters such as pore size, porosity and thickness of porous substrate have a crucial effect on CIS performance, which determines whether the water sublimator can work normally. When the cone height is 1.5 mm, the cone angle is 60° and the FW's inlet pressure is 26 kPa, according to the studies in the references [20,21], the target of PAFS's pore size is 350 μm, and the appropriate pore size of SSPD needs to be further studied, we determined the data range shown in the Table 2 [20,21].

**Table 2.** Structural parameters of porous substrate varied in the numerical study.

SSPD's Porosity	SSPD's Pore Size (μm)	PAFS's Porosity	PAFS's Pore Size (μm)
0.1–0.8	15	0.3	200
0.3	5–40	0.3	200
0.3	15	0.1–0.8	200
0.3	15	0.3	50–350

#### 2) Flow characteristics and fluid properties

The flow characteristics and fluid properties include viscosity, the inlet flow velocity of the thermal loop and the inlet pressure of the FW loop. The viscosity of the FW and the WF is an important physical parameter. When the loop structure is determined, the variation of viscosity with temperature will cause the change of pressure loss and directly affect the operating cost of the system.

The FW's inlet pressure The FW's inlet pressure directly determines the pressure distributed in the PAFS, and the flow rate of the WF in the thermal loop determines the heat input per unit time of CIS. All these factors affect the performance of CIS, and when they exceed the allowed range, they may cause the breakthrough phenomenon of the CIS. Flow characteristics and fluid properties varied in the numerical study is presented in Table 3.

**Table 3.** Flow characteristics and fluid properties varied in the numerical study.

WF's Viscosity (mPa/s)	WF's Flow Rate (m/s)	FW Viscosity (mPa/s)	FW Inlet Pressure (KPa)
0.9–1.4	0.761	1.0828	26
1.3077	0.6–0.9	1.0828	26
1.3077	0.761	0.8–1.3	26
1.3077	0.761	1.0828	24–28

#### 3) Layout of the orifice

The layout of the orifice influences the FW's diffusion in porous substrate and thereby affects the uniformity of temperature distribution in the porous substrate. Two kinds of the orifice layout are designed for comparative analysis, as shown in Figure 4. In case A, four orifices are arranged symmetrically, and each orifice provides FW to the corresponding SSPD. In case B, two orifices are a group, and they supply FW to a SSPD together.

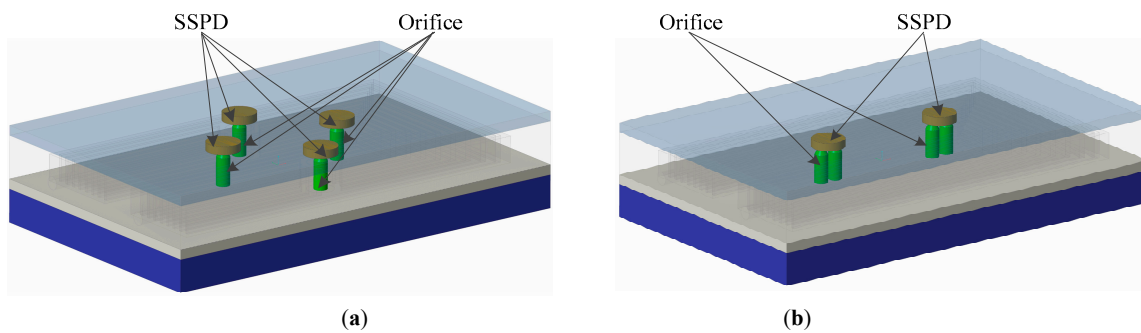


**Figure 4.** Layout of the orifice in the FW loop. (a) Case A: the layout of the orifice is in the shape of cross. (b) Case B: the orifice is arranged in a straight line.

#### 4) Structure parameters of orifice

The orifice is the connection channel for the FW box and the porous substrate. Its structure size directly affects the inlet pressure and the diffusivity of the FW, so far, the investigation did not appear in the literature. When the porosity and the pore size of the PAFS are 0.3 and 15  $\mu\text{m}$  respectively, the porosity and the pore diameter of the SSPD are 0.3 and 200  $\mu\text{m}$ , the influence of cone height and cone angle on heat and mass transfer is studied. The setting of the cone height, cone angle and inlet pressure of the FW loop are shown in Table 4.

**Table 4.** Conditions for the numerical investigation.

Cone Height (mm)	Cone Angle ( $^{\circ}$ )	FW Inlet Flow Velocity (m/s)
1.5-2-2.5-3	60	0.00283
2	20-30-40-50-60	0.00283

### 3. Research Results and Discussion

Performing numerical calculations on different grid sizes ensure a grid independent solution. The grid independence of outlet temperature (Figure 5a) and inlet pressure (Figure 5b) under different inlet temperatures of the WF was checked. Four grid sizes are considered from 60,853 to 283,443. It can be seen clearly that the deviation between the simulation results for 60853 and 283443 grids is negligible. Therefore, in this study, 283,443 grids are used to research all the examples.

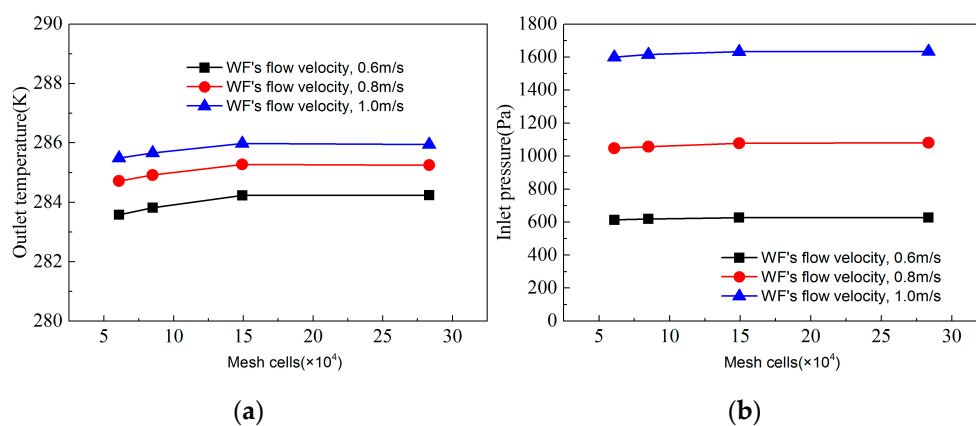


**Figure 5.** Grid independent analysis of simulated outlet temperature and inlet pressure of the WF in different mesh cells. (a) Grid independent analysis of outlet temperature. (b) Grid independent analysis of inlet pressure.

### 3.1. Impact of Physical Parameters of Porous Substrates on the CIS

The impact of the physical parameters of PAFS and SSPD on the pressure field of the FW loop is presented in Figure 6. According to the distribution characteristics of the FW's pressure field, it is more instructive to study the maximum pressure of each section, so the pressure and pressure difference in Figure 6 are measured by the maximum pressure.

The decrease of the PAFS's pressure difference with the increase of the PAFS's pore diameter is showed in Figure 6a. When the PAFS's pore diameter is larger than 10  $\mu\text{m}$ , its impact on the PAFS's pressure difference becomes weaker. When the pore diameter is less than 10  $\mu\text{m}$ , with the decrease of pore diameter, the pressure difference increase rapidly, which also decrease the SSPD's pressure difference and increase the FW's inlet pressure obviously.

Figure 6b shows that SSPD's pore diameter has a little impact on the PAFS's pressure difference, but it determines the SSPD's pressure difference heavily. It can be observed that SSPD's pressure difference accounts for a large proportion in the FW's inlet pressure, and the two curves coincide approximately in the Figure. There is a turning point on the relation curve between the SSPD's diameter and the SSPD's pressure difference, the point is between 10  $\mu\text{m}$  and 15  $\mu\text{m}$ . When the pressure range of the FW's inlet pressure is 20 kPa to 50 kPa, the corresponding SSPD's pore diameter range is 10  $\mu\text{m}$  to 15  $\mu\text{m}$ , which is the reasonable value in this paper.

When the PAFS's porosity is less than 0.2, it has a great influence on the PAFS's pressure difference, which is depicted in Figure 6c. When the PAFS's porosity is between 0.2–0.3, the influence is moderate and suitable for design.

SSPD's porosity also has a great impact on the SSPD's pressure difference, which directly affects the order of magnitude of water pressure, and there is a turning point of the porosity between 0.3 and 0.4, as are displayed in Figure 6d.

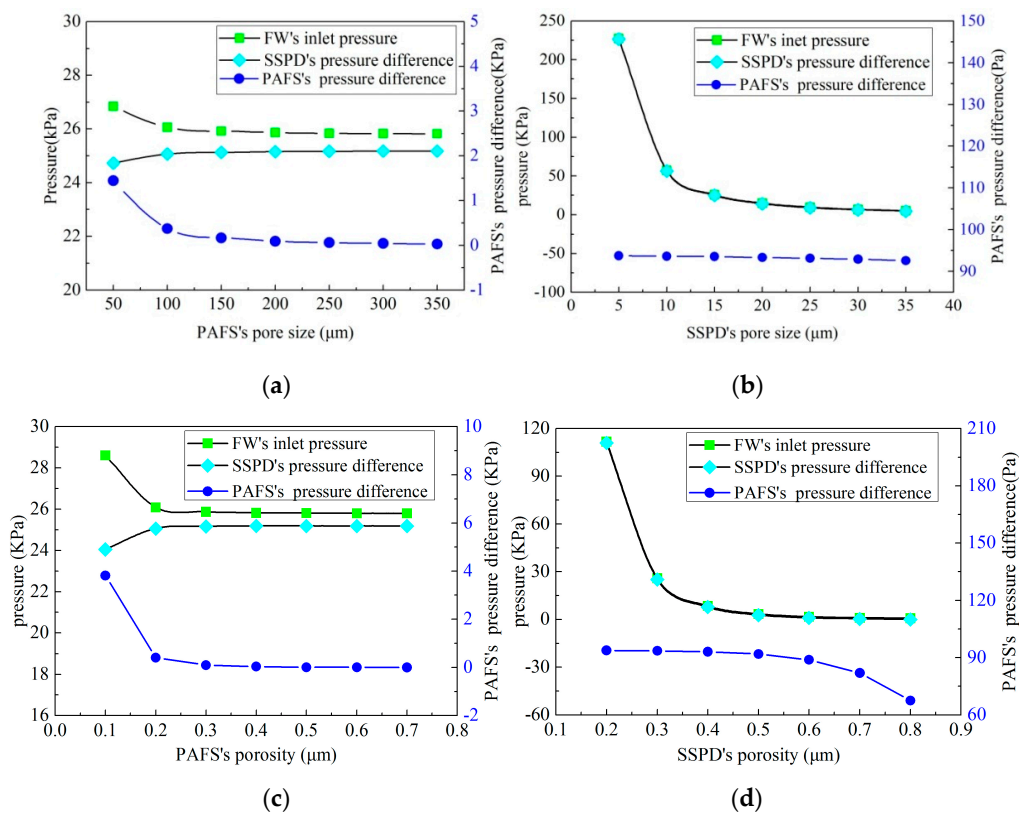


**Figure 6.** Impact of physical parameters of the porous materials on the FW's inlet pressure (a) Impact of the PAFS's pore size on the pressure. (b) Impact of the SSPD's pore size on the pressure. (c) Impact of the PAFS's porosity on the pressure. (d) Impact of the SSPD's porosity on the pressure.

### 3.2. Impact of the Flow Characteristics and Fluid Properties on the CIS

Figure 7 illustrates the impacts of the WF's viscosity and flow velocity on the CIS. It can be clearly seen from Figure 7a that the WF's inlet pressure increased linearly when the WF's viscosity was from 0.9 mPa/s to 1.4 mPa/s. According to hydrodynamics, when the inlet flow velocity is constant, the pressure increase in the inlet will result in an increase in the operating power of the thermal loop.

Figure 7b shows that the WF's inlet pressure increased dramatically as the WF's flow velocity increased from 0.5 m/s to 1.0 m/s, which makes the mechanical pump in the thermal loop potentially overloaded. For the reliable operation of the thermal loop, the power of the pump should be appropriately increased.

The CP's outlet temperature rose nonlinearly with the WF's flow velocity, as shown in Figure 7c, while the temperature difference between the CP's inlet and outlet gradually decreases, as Figure 7d shows. According to the thermodynamic, the flow velocity disturbance affects the CP's outlet temperature, and then the temperature of the spacecraft applications.

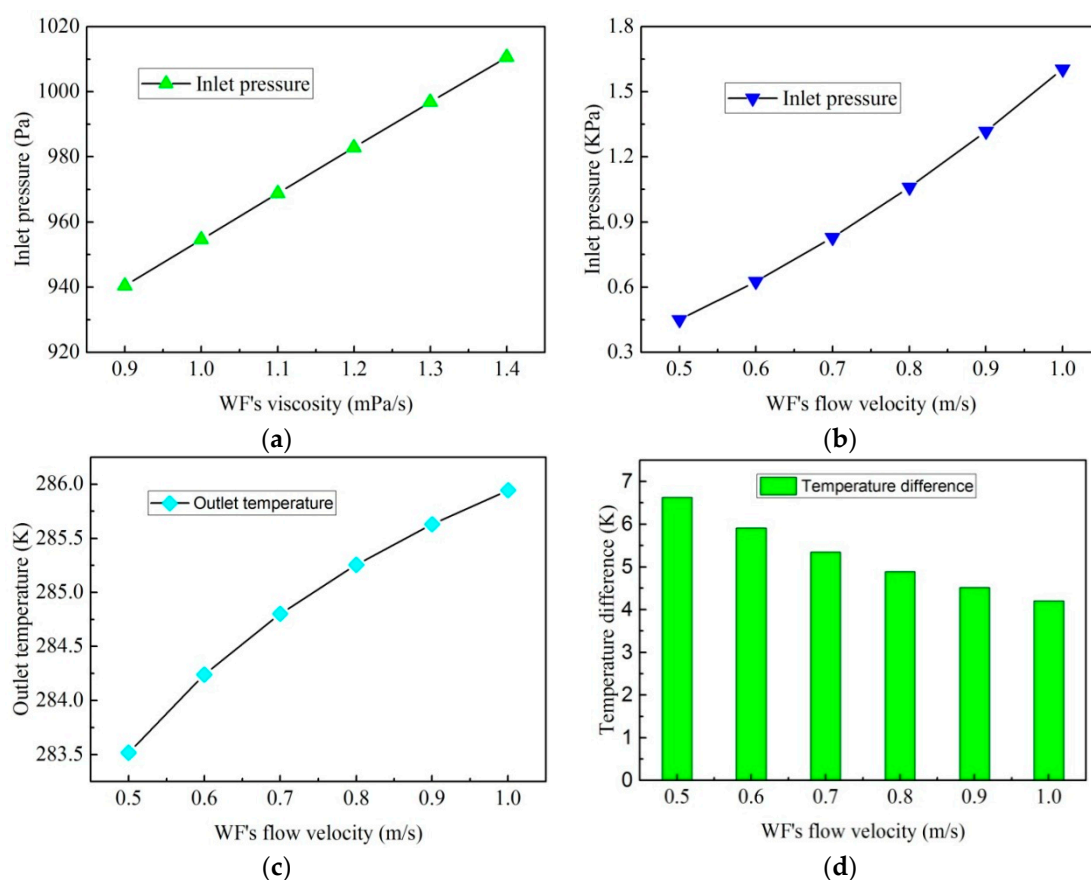


**Figure 7.** Plots of the WF's viscosity and flow velocity on the inlet pressure and the outlet temperature; (a) Impact of the WF's viscosity on the inlet pressure, (b) Impact of the WF's flow velocity on the inlet pressure, (c) Impact of the WF's flow velocity on the outlet temperature, and (d) Impact of the WF's flow velocity on the temperature difference between the inlet and the outlet.

The influence curves of the viscosity and the FW's inlet pressure on the FW loop are drawn in Figure 8.

Figure 8a indicates the trend of the inlet pressure with the FW's viscosity. It can be seen from the curve diagram that the inlet pressure increases by 60 percent when the FW's viscosity rises from 1.0 mPa/s to 1.6 mPa/s. The influence of the FW's inlet pressure disturbance on the inlet flow velocity is showed in Figure 8b. In the curve, the inlet flow velocity increases linearly with the increase of the

inlet pressure, and in the variation range of the inlet pressure, the flow velocity rises by 24 percent. These results imply that the influence of the viscosity on CIS should be considered in CIS design.

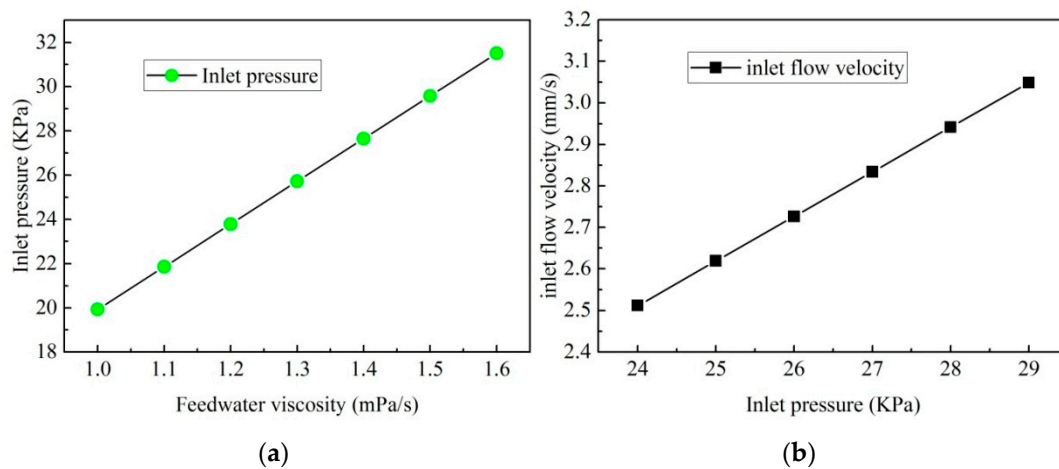


**Figure 8.** Plots of the viscosity and FW's inlet pressure on the inlet pressure and the inlet flow velocity; (a) Impact of the WF's flow velocity on the inlet pressure, (b) Impact of the WF's viscosity on the inlet pressure.

### 3.3. Impact of the Layout of the Orifice on the CIS

The temperature distribution of the CIS under two orifice layouts is drawn in Figure 9. According to the temperature indicated by the color, it can be known that the PAFS is the place where water sublimation occurs, and the temperature is the lowest. The WF's temperature at the inlet of the CP is the highest. As the WF continuously dissipates heat to the CIS, the WF's temperature drops at the outlet of the CP. In Figure 9a, the inlet temperature is 290.15 K, the outlet temperature is 284.96 K, and the temperature decreases by 5.19 K. In Figure 9b, the inlet temperature is 290.15 K, the outlet temperature is 285.09 K, and the temperature is 5.06 K lower. These results suggest that the cooling effect of the two structures is pretty similar, and the cooling temperature difference is less than 3%.

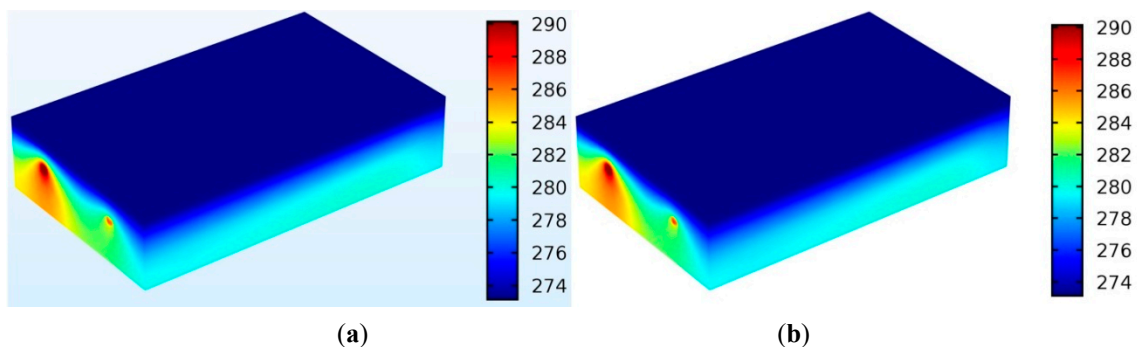


**Figure 9.** Temperature field in different layout of the orifice; (a) The temperature field with the orifice layout in cross, and (b) The temperature field with the orifice layout in line.

Due to the structure of the CP's cooling-channel, the heat resistance between the heat source and the cold source inside the CIS is uneven, which will inevitably make the temperature distribution uneven on each section in the CIS and will affect the melting speed of the ice at different positions on the sublimation interface, and may induce the breakthrough phenomenon of the ice. Therefore, to investigate the temperature distribution inside the CIS, three sections were selected from the two structures respectively, as the Figure 10 shows. The three sections are located at the SSPD's top, the SSPD's bottom and the top of the CP's cooling-channel.

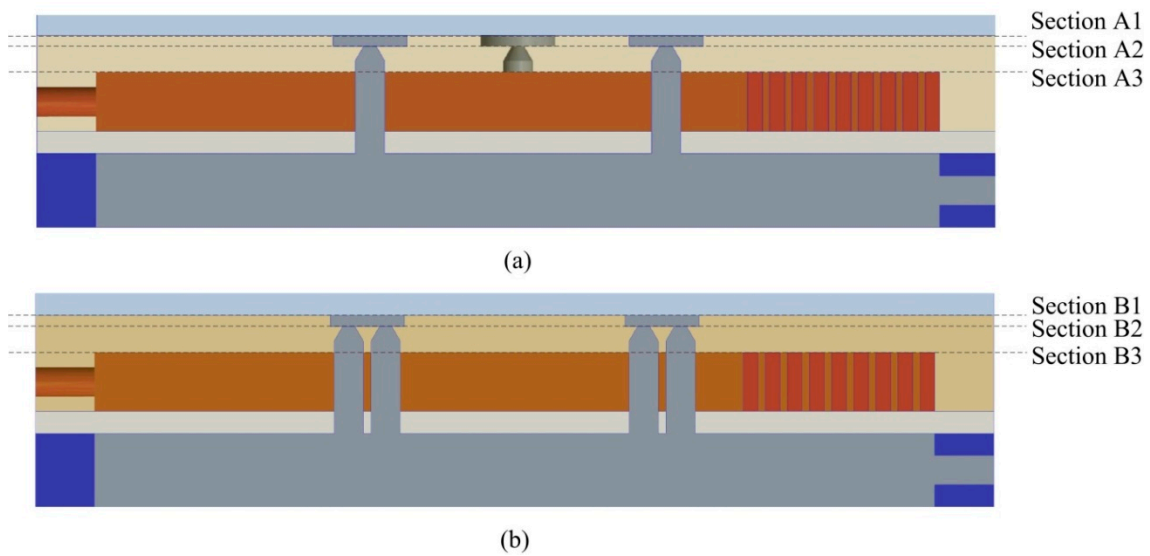


**Figure 10.** Layout of the section (a) The sections in the CIS with the orifice layout in cross. (b) The sections in the CIS with the orifice layout in line.

Figure 11 shows the temperature distribution on different sections in the two CIS with different orifice layout. The 3D colormap surfaces of the sections inside the two CIS are different. For example, in Figure 11a,c,e, there are five peaks, while in Figure 11b,d,f, there are only three peaks. These peaks locate at the CP’s inlet, the corner of the CP’s channel and the orifice among the CP’s channel respectively. In these three types of places, the structure of the CP’s channel changes, which changes the WF’s flow-status, and the heat transfer efficiency has been increased.

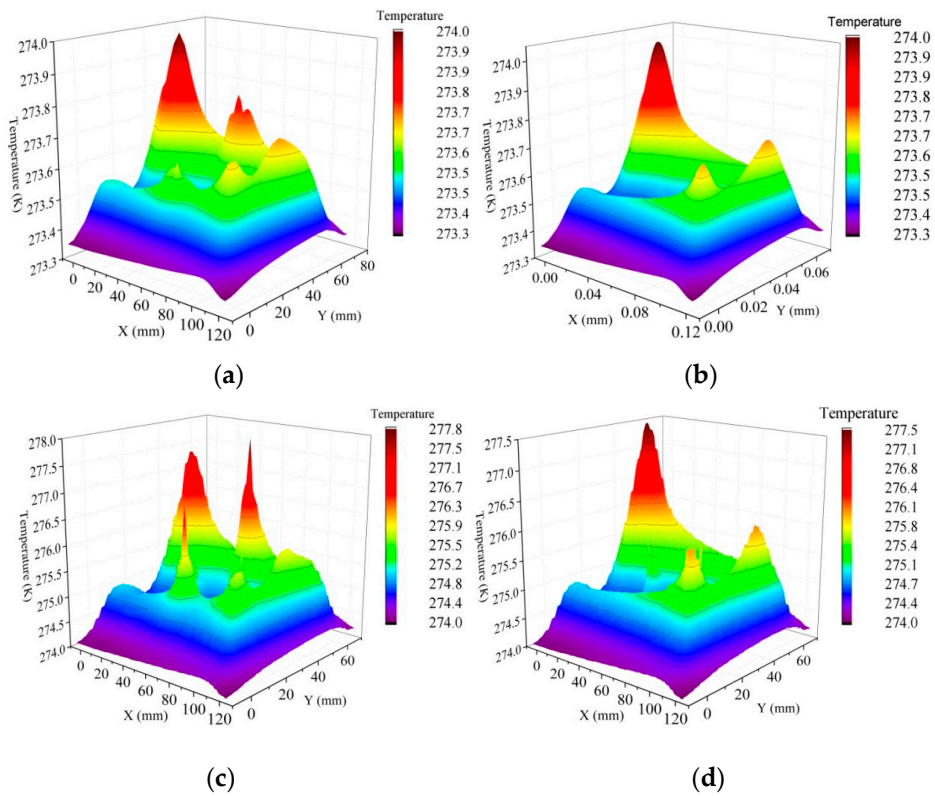


**Figure 11.** Cont.

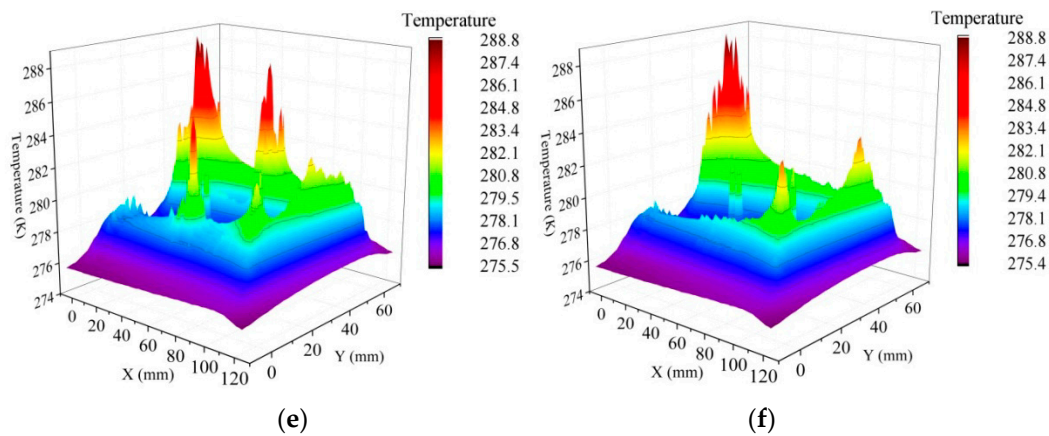


**Figure 11.** The temperature distribution on the sections (a) The temperature distribution on the section A1. (b) The temperature distribution on the section B1. (c) The temperature distribution on the section A2. (d) The temperature distribution on the section B2. (e) The temperature distribution on the section A3. (f) The temperature distribution on the section B3.

The maximum and minimum temperatures on the corresponding sections are nearly equal when comparing each Figure, however these result can't clarify the uneven degree of temperature on the sections. Table 5 lists the temperature uniformity of the sections. It can be seen from these data that the temperature uniformity gradually increases as the section gets close to the cold source, and the temperature uniformity of the CIS with the orifice layout in cross is a little better than that of the CIS with the orifice layout in line.

**Table 5.** Uniformity coefficients of the sections.

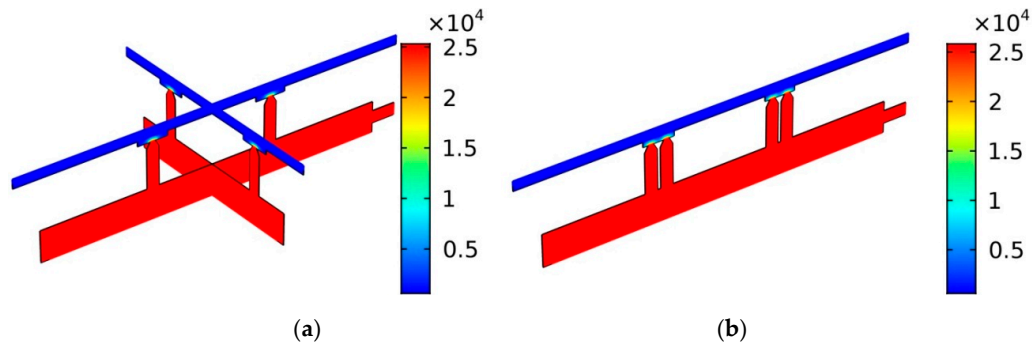
Sections	Maximum Temperature (K)	Minimum Temperature (K)	Average Temperature (K)	Temperature Uniformity Coefficient
Section A1	273.9806398	273.3429304	273.5334432	0.997669
Section A2	278.1846081	274.0394413	274.9725135	0.984925
Section A3	288.7247784	275.5876286	278.3014317	0.952795
Section B1	274.0029072	273.3385126	273.5240334	0.997571
Section B2	277.4333061	274.0194208	274.9176216	0.987582
Section B3	288.7316393	275.5344049	278.1660873	0.952556

From the above, there is a great difference of the temperature distribution on each section, but the minimum temperature and the maximum temperature on the corresponding sections are similar. The closer the section is to the sublimation interface, the larger the temperature uniformity is. The value of the temperature uniformity of case A is slightly less than that of case B.

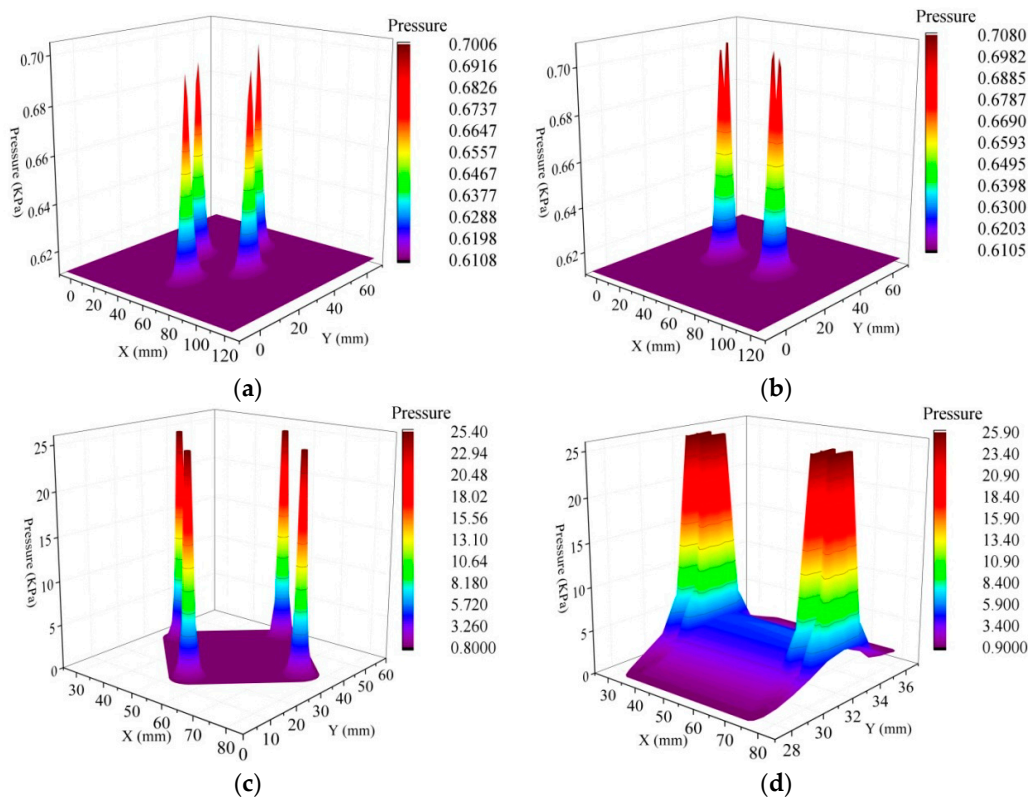
The pressure distribution of the FW in the two types of CIS is showed in Figure 12. From Figure 12a,b, it can be observed that the SSPD divides the FW into two zones: high pressure and low pressure. The FW between the FW inlet and the bottom surface of the SSPD is regarded as the high pressure zone, while the FW between the top surface of the SSPD and the top surface of the PAFS belongs to low pressure zone. The pressure drop from the FW inlet to the sublimation interface is mainly on the SSPD, which perfectly realizes the separation of the pressure control from the water sublimation and sublimate the FW in the PAFS.

Figure 13 shows the pressure distribution on the sections. There are four separate peaks in the Figure 13a,c, while synchronously Figure 13b,d each have two saddle-shaped peaks. These results imply that the pressure distribution is correlated with the layout of the orifice, as well as that the pressure at the place of the orifice is higher than the surrounding pressure. The pressure uniformity coefficients (PUC) of the sections are list in the Table 6. On the basis of these datum, it is easy to

understand that the PUC increases significantly with the action of the SSPD, and it can be concluded that the PUC on the sublimation interface of the PAFS is relatively high, which is conducive to avoid the breakthrough of the ice.



**Figure 12.** FW's pressure field (a) The FW's pressure field in the CIS with the orifice layout in cross. (b) The FW's pressure field in the CIS with the orifice layout in line.



**Figure 13.** Pressure distribution on the sections. (a) The pressure distribution on the section A1. (b) The pressure distribution on the section B1. (c) The pressure distribution on the section A2. (d) The pressure distribution on the section B2.

**Table 6.** PUC of the sections.

Sections	Maximum Temperature (K)	Minimum Temperature (K)	Average Temperature (K)	Pressure Uniformity Coefficient
Section A1	700.58955	610.9999994	612.0034769	0.853612673
Section A2	25,328.703	862.8228082	25,094.28682	0.025041801
Section B1	707.63275	611	612.0040322	0.842104398
Section B2	25,866.459	927.8483014	25,357.44003	0.016517032

### 3.4. Impact of the Structure Parameters of the Orifice on the CIS

The relation between the cone angle of the orifice as well as the FW's inlet pressure is drawn in Figure 14a. The FW's inlet pressure increases nonlinearly with the increase of the cone angle of the orifice. The inlet pressure rises slightly when the cone angle is from 20° to 40°, nevertheless when the cone angle is from 40° to 60°, the inlet pressure goes up memorably. The applicable inlet pressure of the FW should be greater than 20 kPa, as a consequence the suitable value range of the cone angle is from 50° to 60° in this paper.

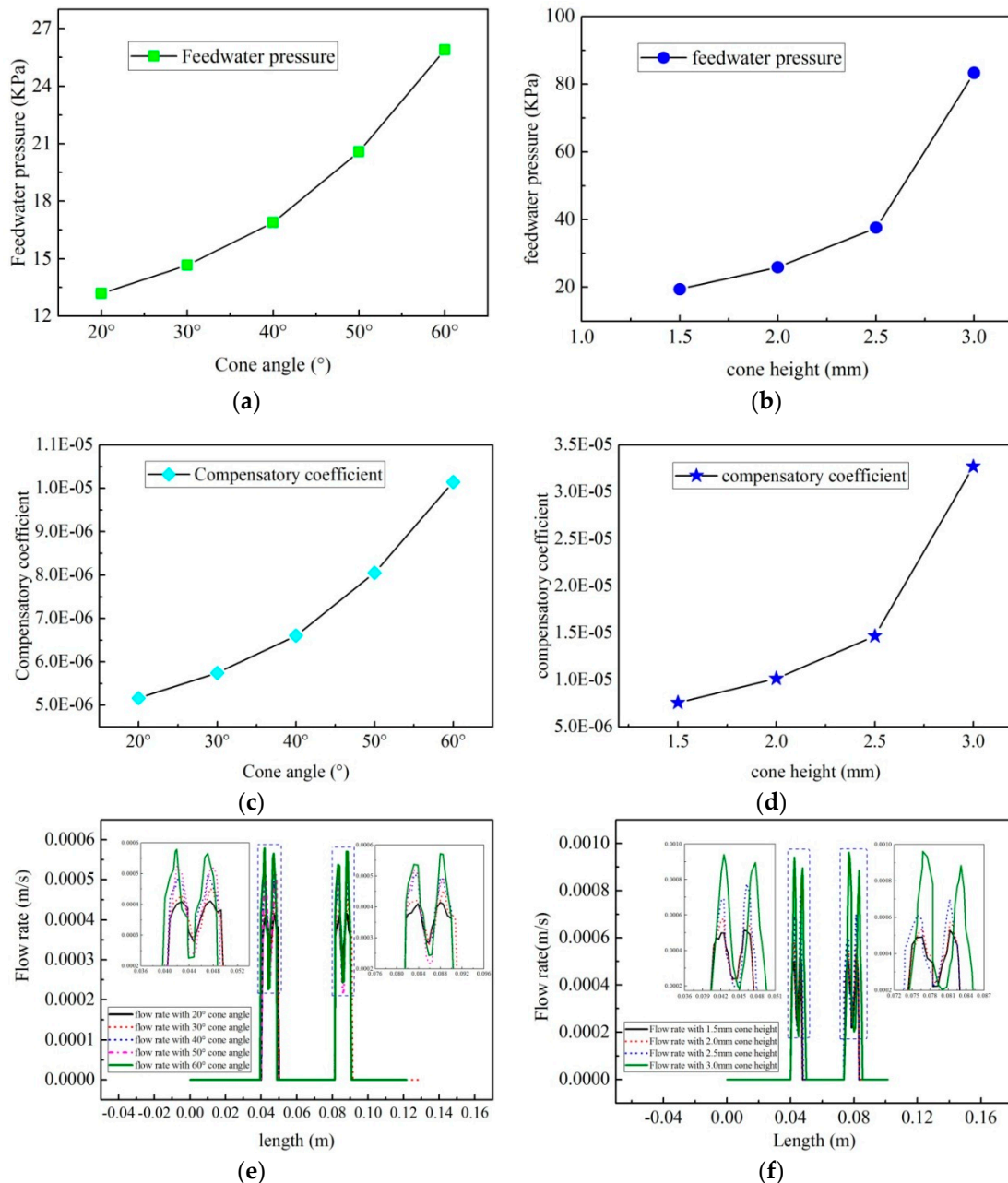


**Figure 14.** Plots of the cone height and the cone angle on the FW inlet pressure (a) Impact of the cone angle on the FW's inlet pressure. (b) Impact of the cone height on the FW's inlet pressure. (c) Impact of the cone angle on the compensatory coefficient. (d) Impact of the cone height on the compensatory coefficient. (e) Impact of the cone angle on the flow velocity on the symmetric line on section B1. (f) Impact of the cone height on the flow velocity on the symmetric line on section B1.

The curve of the FW's inlet pressure changing with the cone height is shown in Figure 14b, when the cone angle of the orifice is at  $60^\circ$ . With the increase of the cone height, the FW's inlet pressure rises gradually. On the basis of the hydrodynamics, this result is mainly caused by the decrease of the flow-area of the orifice when the cone height increases under the condition of constant cone angle. In the light of the literatures investigation and the relation in the curve of the Figure 14b, the range of cone height from 1.5 mm to 2.0 mm could satisfy the design requirement of the CIS.

Figure 14c,d show the curves of the compensatory coefficient VS the cone angle and the cone height in the orifice. It should be noted that the curves in Figure 14a,c have the same trends, while the curves in Figure 14b,d also have the same trends, mainly because the operating power of the FW loop increases with the FW's inlet pressure.

The curves of the flow velocity on the symmetric line of the section B1 VS the cone angle and the cone height of the orifice are shown in Figure 14e,f, respectively. The curves depict that the maximum temperatures on the symmetric increase with the cone angle and the cone height. When the cone angle is from  $20^\circ$  to  $60^\circ$ , the increase of the flow velocity is lower that when the cone height is from 1.5 mm to 3.0 mm. As a result, the cone height has a greater impact on the maximum flow velocity than that of the cone angle in the research of this paper.

To sum up, the influence of cone height on the compensation coefficient, FW pressure and the maximum flow velocity of Section 4 is far greater than that of the cone angle. According to the calculation and analysis results, the appropriate range of the cone height is from 1.5 mm to 2 mm.

### 3.5. Data Validity

The COMSOL Multiphysics software has been successfully applied to numerical studies of heat and mass transfer in various applications, which can be referred to in the literature [53–57]. In this paper, the setting of boundary conditions and initial conditions is consistent with or approximate to the setting of reference [20,21,23,24,26,27], which is reasonable. According to the principle of energy conservation, the temperature drop value of the WF is set at 5 K, which is very close to the value calculated by the software under the boundary conditions and initial conditions specified above. The comparison shows the rationality of the simulation results.

## 4. Conclusions

In this paper, the CIS development unit model, the mathematical models of heat and mass transfer and the evaluation coefficient were presented to investigate the reliability issues generated by large temperature or pressure difference. The influences of the physical properties of the porous substrate, physical properties of the working fluid, orifice layouts and orifice-structure parameters on the characteristics of flow field and temperature field were analyzed. The following main results were obtained:

- 1) There are turning points in the influence curve of the porous-substrate physical parameters on the FW pressure. The SSPD's pore diameter and porosity should be below the value of the turning point in order to control the FD's pressure. On the contrary, the value of the PAFS's pore diameter and porosity should be larger than that of the turning point, so as to reduce the influence on pressure, increase the pore size and improve the contaminant insensitivity of CIS.
- 2) The variation of the FW's dynamic viscosity has a significant influence on the FW's pressure, which should be considered when the CIS is designed and used. For example, we can choose an appropriate control strategy to control the flow rate to compensate for the change in viscosity.
- 3) The pressure drop of the FD loop mainly occurs in the SSPD, which fully demonstrate the SSPD's control effect on the FW's pressure. The pressure uniformity coefficients on the AFPS's bottom surfaces are 0.853612673 and 0.842104398 in the two CIS's layout respectively. At the same time, the temperature uniformity coefficients on the same sections are 0.997669 and 0.997571. These

results show that CIS have excellent temperature uniformity and pressure uniformity, but the effect of pressure on the ice breakthrough needs to be noted.

- 4) The cone height of the orifice has a great influence on the FW pressure and the compensation coefficient. The selection of cone height should ensure that sublimation occurs in PAFS, and take into account the running power of the FW loop.

In conclusion, all the rules and results above can not only guide the selection of parameters when designing CIS but also provide methods and data platform for the CIS design or the subsequent studies of the CIS.

**Author Contributions:** Conceptualization, Y.L.; methodology, L.G.; software, L.G.; validation, H.X. and M.Y.; formal analysis, X.Z.; investigation, L.G.; resources, X.N.; data curation, L.G.; writing—original draft preparation, L.G.; writing—review and editing, L.G.; visualization, L.G.; supervision, Y.L.; project administration, Y.L.; funding acquisition, X.N.

**Funding:** This research was funded by National Nature Science Foundation of China through grant no.11472040.

**Conflicts of Interest:** The authors declare no conflict of interest.

## References

1. Singer, J.; Pelfrey, J.; Norris, G. Enabling Science and Deep Space Exploration Through Space Launch System Secondary Payload Opportunities. In Proceedings of the SpaceOps 2016 Conference, Kaejeon, Korea, 16–20 May 2016. [\[CrossRef\]](#)
2. Lapointe, M.R.; Mikellides, P.G.; Reddy, D. High Power MPD Thruster Development at the NASA Glenn Research Center. In *AIAA 2001-3499, 37th Joint Propulsion Conference and Exhibit, Salt Lake City, UT, USA*; AIAA: Reston, VA, USA. [\[CrossRef\]](#)
3. Tang, D.; Xiao, H.; Kong, F.; Deng, Z.; Jiang, S.; Quan, Q. Thermal Analysis of the Driving Component Based on the Thermal Network Method in a Lunar Drilling System and Experimental Verification. *Energies* **2017**, *10*, 355. [\[CrossRef\]](#)
4. Tian, Y.; Deng, Z.-Q.; Tang, D.-W.; Chen, J.-K. Drilling Power Consumption Analysis of Coring Bit in Lunar Sample Mission. *J. Aerosp. Eng.* **2017**, *30*, 04017055. [\[CrossRef\]](#)
5. Kobrick, R.L.; Agui, J.H. Preparing for planetary surface exploration by measuring habitat dust intrusion with filter tests during an analogue Mars mission. *Acta Astronaut.* **2019**, *160*, 297–309. [\[CrossRef\]](#)
6. Xu, H.; Wang, J.; Li, Y.; Bi, Y.; Gao, L. A Thermoelectric-Heat-Pump Employed Active Control Strategy for the Dynamic Cooling Ability Distribution of Liquid Cooling System for the Space Station's Main Power-Cell-Arrays. *Entropy* **2019**, *21*, 578. [\[CrossRef\]](#)
7. Piedra, S.; Torres, M.; Ledesma, S. Thermal Numerical Analysis of the Primary Composite Structure of a CubeSat. *Aerospace* **2019**, *6*, 97. [\[CrossRef\]](#)
8. Gadalla, M.; Ghommem, M.; Bourantas, G.; Miller, K. Modeling and Thermal Analysis of a Moving Spacecraft Subject to Solar Radiation Effect. *Processes* **2019**, *7*, 807. [\[CrossRef\]](#)
9. Skoog, A.I.; Abramov, I.P.; Stoklitsky, A.Y.; Doodnik, M.N. The Soviet-Russian space suits a historical overview of the 1960's. *Acta Astronaut.* **2002**, *51*, 113–131. [\[CrossRef\]](#)
10. Bagiorgas, H.S.; Mihalakakou, G. Experimental and theoretical investigation of a nocturnal radiator for space cooling. *Renew. Energy* **2008**, *33*, 1220–1227. [\[CrossRef\]](#)
11. Roy, S.K.; Avanic, B.L. Optimization of a space radiator with energy storage. *Int. Commun. Heat Mass Transf.* **2006**, *33*, 544–551. [\[CrossRef\]](#)
12. Cuco, A.P.C.; de Sousa, F.L.; Vlassov, V.V.; da Silva Neto, A.J. Multi-objective design optimization of a new space radiator. *Optim. Eng.* **2011**, *12*, 393–406. [\[CrossRef\]](#)
13. Zhong, M.-L.; Li, Y.-Z.; Guo, W.; Wang, S.-N.; Mao, Y.-F. Dynamic in-loop performance investigation and efficiency-cost analysis of dual heat sink thermal control system (DHS-TCS) with a sublimator for aerospace vehicles. *Appl. Therm. Eng.* **2017**, *121*, 562–575. [\[CrossRef\]](#)
14. Metts, J.G.; Klaus, D.M. First-order feasibility analysis of a space suit radiator concept based on estimation of water mass sublimation using Apollo mission data. *Adv. Space Res.* **2012**, *49*, 204–212. [\[CrossRef\]](#)
15. Moller, P.; Loewens, R.; Abramov, I.P.; Albats, E.A. EVA Suit 2000: A joint European/Russian space suit design. *Acta Astronaut.* **1995**, *36*, 53–63. [\[CrossRef\]](#)

16. Skoog, A.I.; Abramov, I.P. EVA 2000: A European/Russian space suit concept. *Acta Astronaut.* **1995**, *36*, 35–51. [[CrossRef](#)]
17. Planert, C.; Kremer, P.; Witt, J. Development of Sublimator Technology for the European EVA Space Suit. In Proceedings of the 21st International Conference on Environmental Systems, San Francisco, CA, USA, 15–18 July 1991; Technical Paper 911577; SAE: Warrendale, PA, USA, 1991. [[CrossRef](#)]
18. Tongue, S.; Swartley, V.; Dingell, C. The Porous Plate Sublimator as the X-38/CRV (Crew Return Vehicle) Orbital Heat Sink. In Proceedings of the 27th International Conference on Environmental Systems, Lake Tahoe, NV, USA, 14–17 July 1997; SAE Technical Paper 972411; SAE: Warrendale, PA, USA, 1997. [[CrossRef](#)]
19. Tongue, S.; Dingell, C. The Porous Plate Sublimator as the X-38/CRV (Crew Return Vehicle) Orbital Heat Sink. In Proceedings of the 27th International Conference on Environmental Systems, Denver, CO, USA, 12–15 July 1999; SAE Technical Paper 1999-01-2004; SAE: Warrendale, PA, USA, 1999. [[CrossRef](#)]
20. Leimkuehler, T.; Anderson, M.; Westheimer, D. Development of a Contaminant Insensitive Sublimator. In Proceedings of the 36th International Conference on Environmental Systems, Norfolk, VA, USA, 17–20 July 2006; SAE Technical Paper 2006-01-2217; SAE: Warrendale, PA, USA, 2006. [[CrossRef](#)]
21. Leimkuehler, T.; Stephan, R. Development and Testing of the Contaminant Insensitive Sublimator. In Proceedings of the 37th International Conference on Environmental Systems, Chicago, IL, USA, 9–12 July 2006; SAE Technical Paper 2007-01-3203; SAE: Warrendale, PA, USA, 2006. [[CrossRef](#)]
22. Leimkuehler, T.; Abounasr, O.; Stephan, R. Design of a Sublimator Driven Coldplate Development Unit. *SAE Int. J. Aerosp.* **2009**, *1*, 532–536. [[CrossRef](#)]
23. Sheth, R.; Stephan, R.; Leimkuehler, T. *Testing and Model Correlation of Sublimator Driven Coldplate Coupons and EDU*; SAE Technical Paper 2009-01-2479; SAE: Warrendale, PA, USA, 2009. [[CrossRef](#)]
24. Leimkuehler, T.; Sheth, R.; Stephan, R. Investigation of Transient Sublimator Performance. In Proceedings of the 39th International Conference on Environmental Systems, Savannah, GA, USA, 12–16 July 2009; SAE Technical Paper 2009-01-2480; SAE: Warrendale, PA, USA, 2009. [[CrossRef](#)]
25. Sheth, R.; Stephan, R.; Leimkuehler, T. Experimental Investigation of Sublimator Performance at Transient Heat Loads. In Proceedings of the 42nd International Conference on Environmental Systems, San Diego, CA, USA, 15–19 July 2012. [[CrossRef](#)]
26. Sheth, R.B.; Stephan, R.A.; Leimkuehler, T.O. Sublimator Driven Coldplate Engineering Development Unit Test Results. In Proceedings of the 40th International Conference on Environmental Systems, Barcelona, Spain, 11–15 July 2010. [[CrossRef](#)]
27. Sheth, R.B.; Stephan, R.A.; Leimkuehler, T.O. Investigation of Transient Performance for a Sublimator. In Proceedings of the 40th International Conference on Environmental Systems, Barcelona, Spain, 11–15 July 2010. [[CrossRef](#)]
28. Leimkuehler, T.; Kennedy, S. An Integrated Sublimator Driven Coldplate. In Proceedings of the 41st International Conference on Environmental Systems, Portland, OR, USA, 17–21 July 2011. [[CrossRef](#)]
29. Wang, Y.Y.; Zhong, Q.; Li, J.D.; Ning, X.W. Numerical and experimental study on the heat and mass transfer of porous plate water sublimator with constant heat flux boundary condition. *Appl. Therm. Eng.* **2014**, *67*, 469–479. [[CrossRef](#)]
30. Tan, X.; Chen, W.; Wu, G.; Yang, J. Numerical simulations of heat transfer with ice–water phase change occurring in porous media and application to a cold-region tunnel. *Tunn. Undergr. Space Technol.* **2013**, *38*, 170–179. [[CrossRef](#)]
31. Huang, P.C.; Yang, C.F.; Chang, S.-Y. Mixed Convection Cooling of Heat Sources Mounted with Porous Blocks. *J. Thermophys. Heat Transf.* **2004**, *18*, 464–475. [[CrossRef](#)]
32. Kolunin, V.S. Heat and mass transfer in porous media with ice inclusions near the freezing-point. *Int. J. Heat Mass Transf.* **2005**, *48*, 1175–1185. [[CrossRef](#)]
33. Tan, X.; Chen, W.; Tian, H.; Cao, J. Water flow and heat transport including ice/water phase change in porous media: Numerical simulation and application. *Cold Reg. Sci. Technol.* **2011**, *68*, 74–84. [[CrossRef](#)]
34. Wang, W.; Yang, J.; Hu, D.; Pan, Y.; Wang, S.; Chen, G. Experimental and numerical investigations on freeze-drying of porous media with prebuilt porosity. *Chem. Phys. Lett.* **2018**, *700*, 80–87. [[CrossRef](#)]
35. Ganguly, S. Exact Solution of Heat Transport Equation for a Heterogeneous Geothermal Reservoir. *Energies* **2018**, *11*, 2935. [[CrossRef](#)]
36. Deng, Z.; Liu, X.; Huang, Y.; Zhang, C.; Chen, Y. Heat Conduction in Porous Media Characterized by Fractal Geometry. *Energies* **2017**, *10*, 1230. [[CrossRef](#)]

37. Hanlon, M.; Ma, H. Evaporation Heat Transfer in Sintered Porous Media. In Proceedings of the 8th AIAA/ASME Joint Thermophysics and Heat Transfer Conference, St. Louis, MI, USA, 24–26 June 2002. [[CrossRef](#)]
38. Siahpush, A.; O'Brien, J. Heat Transfer Performance of a Porous Metal Foam/Phase Change Material System, Part 2: Melting. In Proceedings of the 9th AIAA/ASME Joint Thermophysics and Heat Transfer Conference, San Francisco, CA, USA, 5–8 June 2006. [[CrossRef](#)]
39. Wang, Z.H.; Shi, M.H. Numerical study on sublimation–condensation phenomena during microwave freeze drying. *Chem. Eng. Sci.* **1998**, *53*, 3189–3197. [[CrossRef](#)]
40. Wu, D.; Lai, Y.; Zhang, M. Heat and mass transfer effects of ice growth mechanisms in a fully saturated soil. *Int. J. Heat Mass Transf.* **2015**, *86*, 699–709. [[CrossRef](#)]
41. Rattanadecho, P. Simulation of melting of ice in a porous media under multiple constant temperature heat sources using a combined transfinite interpolation and PDE methods. *Chem. Eng. Sci.* **2006**, *61*, 4571–4581. [[CrossRef](#)]
42. Wu, H.; Tao, Z.; Chen, G.; Deng, H.; Xu, G.; Ding, S. Conjugate heat and mass transfer process within porous media with dielectric cores in microwave freeze drying. *Chem. Eng. Sci.* **2004**, *59*, 2921–2928. [[CrossRef](#)]
43. Lei, G.; Cao, N.; Liu, D.; Wang, H. A Non-Linear Flow Model for Porous Media Based on Conformable Derivative Approach. *Energies* **2018**, *11*, 2986. [[CrossRef](#)]
44. Yu, S.; Cui, Y.; Shao, Y.; Han, F. Simulation Research on the Effect of Coupled Heat and Moisture Transfer on the Energy Consumption and Indoor Environment of Public Buildings. *Energies* **2019**, *12*, 141. [[CrossRef](#)]
45. Cai, J.; Sun, S.; Habibi, A.; Zhang, Z. Emerging Advances in Petrophysics: Porous Media Characterization and Modeling of Multiphase Flow. *Energies* **2019**, *12*, 282. [[CrossRef](#)]
46. Warning, A.D.; Arquiza, J.M.R.; Datta, A.K. A multiphase porous medium transport model with distributed sublimation front to simulate vacuum freeze drying. *Food Bioprod. Process.* **2015**, *94*, 637–648. [[CrossRef](#)]
47. Farid, M. The moving boundary problems from melting and freezing to drying and frying of food. *Chem. Eng. Process.* **2002**, *41*, 1–10. [[CrossRef](#)]
48. Leung, M.; Ching, W.H.; Leung, D.Y.C.; Lam, G.C.K. Theoretical study of heat transfer with moving phase-change interface in thawing of frozen food. *J. Phys. D Appl. Phys.* **2005**, *38*, 477–482. [[CrossRef](#)]
49. Rattanadecho, P.; Wongwises, S. Simulation of freezing of water-saturated porous media in a rectangular cavity under multiple heat sources with different temperature using a combined transfinite interpolation and PDE methods. *Comput. Chem. Eng.* **2007**, *31*, 318–333. [[CrossRef](#)]
50. Nakagawa, K.; Ochiai, T. A mathematical model of multi-dimensional freeze-drying for food products. *J. Food Eng.* **2015**, *161*, 55–67. [[CrossRef](#)]
51. Machrafi, H.; Lebon, G. Fluid flow through porous and nanoporous media within the prisms of extended thermodynamics: Emphasis on the notion of permeability. *Microfluid. Nanofluid.* **2018**, *22*, 65. [[CrossRef](#)]
52. Wu, K.; Chen, Z.; Li, J.; Li, X.; Xu, J.; Dong, X. Wettability effect on nanoconfined water flow. *Proc. Natl. Acad. Sci. USA* **2017**, *114*, 3358–3363. [[CrossRef](#)]
53. Tenpierik, M.; Wattez, Y.; Turrin, M.; Cosmatu, T.; Tsafou, S. Temperature Control in (Translucent) Phase Change Materials Applied in Facades: A Numerical Study. *Energies* **2019**, *12*, 3286. [[CrossRef](#)]
54. Lei, X.; Zheng, X.; Duan, C.; Ye, J.; Liu, K. Three-Dimensional Numerical Simulation of Geothermal Field of Buried Pipe Group Coupled with Heat and Permeable Groundwater. *Energies* **2019**, *12*, 3698. [[CrossRef](#)]
55. Nyallang Nyamsi, S.; Tolj, I.; Lototsky, M. Metal Hydride Beds-Phase Change Materials: Dual Mode Thermal Energy Storage for Medium-High Temperature Industrial Waste Heat Recovery. *Energies* **2019**, *12*, 3949. [[CrossRef](#)]
56. Zhu, P.; Peng, H.; Yang, J. Analyses of the Temperature Field of a Piezoelectric Micro Actuator in the Endoscopic Biopsy Channel. *Appl. Sci.* **2019**, *9*, 4499. [[CrossRef](#)]
57. Ebrahimi, A.; Kleijn, C.; Richardson, I. Sensitivity of Numerical Predictions to the Permeability Coefficient in Simulations of Melting and Solidification Using the Enthalpy-Porosity Method. *Energies* **2019**, *12*, 4360. [[CrossRef](#)]

